



# A detailed study on the optical performance of parabolic trough solar collectors with Monte Carlo Ray Tracing method based on theoretical analysis



Bin Zou, Jiankai Dong, Yang Yao<sup>\*</sup>, Yiqiang Jiang<sup>\*</sup>

Department of Building Thermal Energy Engineering, Harbin Institute of Technology, Harbin, China

## ARTICLE INFO

### Article history:

Received 30 June 2016

Received in revised form 26 November 2016

Accepted 23 January 2017

### Keywords:

Parabolic trough solar collector

Optical performance

Monte Carlo Ray Tracing

Theoretical analysis

## ABSTRACT

The optical performance of a parabolic trough solar collector (PTC) is studied comprehensively based on Monte Carlo Ray Tracing method (MCRT) and theoretical analysis. The MCRT models are established, and the theoretical equations of several critical parameters are derived firstly. And then the effects of different geometrical parameters on the optical performance are discussed in detail. It is revealed that the distribution of local concentration ratio around the absorber tube changes greatly, and cannot be divided into four parts as previous studies showed for some special parameter conditions. The theoretically derived parameters explain very well the different properties for the critical conditions. The variations of those parameters with different geometrical configurations are further displayed. Accordingly, the optical properties for different critical parameters are discussed. The size relationship between the reflected light cone and the absorber diameter affects the optical efficiency significantly because of the rays escaping effect. Practically, the absorber diameter should be larger than the size of the reflected light cone to avoid great optical loss caused by rays escaping. All the findings in this paper establish the foundation for further research on the optical-to-thermal energy conversion in the PTC system, and provide a reference for designing and optimizing PTC's structure.

© 2017 Published by Elsevier Ltd.

## 1. Introduction

Energy shortage and environmental deterioration, caused by excessively consuming fossil fuels, have become severe issues facing humans over past decades (Geyer, 2007; Kalogirou, 2004; Tian and Zhao, 2013). A promising solution is to exploit and utilize renewable energy resources as the alternatives to fossil fuels, which has attracted extensive attentions (Geyer, 2007; Vijay et al., 2013). As the most widely distributed renewable energy resource, solar energy has been applied in various social industries (Fernandez et al., 2010; Kalogirou, 2004). The parabolic trough solar collector (PTC) technology used in solar power system is the most cost-effective technology for utilization of solar energy (Jebasingh and Joselin-Herbert, 2016; Price et al., 2002). As the most important component, solar collectors have significant effects on the cost and performance of the whole system (Schiel, 2012). Thus, to reduce the cost and enhance the competitiveness of solar power technology to traditional fossil power plants, further improvements of the solar collector is essential.

A parabolic trough solar collector (PTC) focuses the reflected solar rays from the parabolic reflector onto the receiver tube that is located at the focal line. And then the reflected solar radiation is absorbed and converted to thermal energy, and transferred to the heat transfer fluid (HTF) flowing in the absorber tube. The process of the photo-thermal conversion is complex, and the distribution of the solar energy flux on the absorber is the boundary condition for heat transfer calculation (Cheng et al., 2010; Hachicha et al., 2013; He et al., 2011, 2012). Therefore, the optical performance has great effects on the overall performance of the PTC. During 1970s and 1980s, the simplified geometric analysis method was the most widely used method for studying PTCs' optical performance, and some basic properties have been found (Burkhard et al., 1973; Evans, 1977; Nicolas and Duran, 1980; Duran and Nicolas, 1984; Riveros and Oliva, 1986). Later, the integral methods were adopted to improve the results' accuracy (Huang et al., 2012; Jeter, 1986a, 1986b). Buie et al. (2003a, 2003b) developed a calculation model of the sunshape, which was usually used to simulate the real energy intensity distribution of the solar disk in other references. Ray Tracing Method (RTM) was another effective method to be used for optical performance study. Daly (1979) proposed a backward ray tracing method to

<sup>\*</sup> Corresponding authors.

E-mail addresses: [yangyao1963@163.com](mailto:yangyao1963@163.com) (Y. Yao), [jyq7245@sina.com](mailto:jyq7245@sina.com) (Y. Jiang).

### Nomenclature

$A_i$	area of the $i$ th grid ( $\text{m}^2$ )
$CL$	local concentration ratio
$CL_i$	local concentration ratio of the $i$ th grid
$CL_{max}$	maximum local concentration ratio
$CL_{ave}$	average local concentration ratio
$d_a$	absorber tube out diameter (m)
$d_{a,re}$	required diameter of the absorber tube to avoid rays escaping (m)
$d_g$	glass envelope out diameter (m)
$f$	focal length (m)
$I_D$	direct normal solar radiation intensity ( $\text{W}/\text{m}^2$ )
$I_{eff}$	effective solar radiation intensity incident on the aperture ( $\text{W}/\text{m}^2$ )
$I_i$	local energy flux density of the $i$ th grid ( $\text{W}/\text{m}^2$ )
$L_a$	absorber tube length (m)
$N_c$	grid number in the circular direction of the absorber
$N_z$	grid number in the length direction of the absorber
$N_n$	total number of grids
$N_{ray}$	total number of rays
$W$	aperture width (m)

### Greek symbols

$\alpha_a$	absorptivity of the absorber
$\chi$	angle span at the bottom of the absorber without receiving any reflected rays ( $^\circ$ )

$\delta$	radial angle of the sun ( $\delta = 4.65 \text{ mrad}$ )
$\varepsilon$	nonuniformity of solar flux density distribution on the absorber tube
$\phi$	angle for auxiliary calculation ( $^\circ$ )
$\gamma$	intercept factor
$\eta_o$	optical efficiency (%)
$\varphi_a$	circumferential angle of the absorber ( $^\circ$ )
$\varphi_s$	circumferential angle of the point on the solar disk (mrad)
$\theta_s$	radial angle of the point on the solar disk (mrad)
$\rho_r$	reflectivity of the parabolic reflector
$\tau_g$	transmissivity of the glass envelope
$\Omega$	effective angle span receiving concentrated beam ( $^\circ$ )
$\psi$	position angle of the point on the parabolic reflector ( $^\circ$ )
$\psi_{rim}$	rim angle ( $^\circ$ )
$\kappa_1 \sim \kappa_8$	uniformly distributed random number between 0 and 1

### Abbreviations

FVM	Finite Volume Method
HTF	heat transfer fluid
MCM	Monte Carlo Method
MCRT	Monte Carlo Ray Tracing
PTC	parabolic trough solar collector
RTM	Ray Tracing Method

study the energy flux distributions of cylindrical concentrators. However, the method was just for two-dimensional analysis. Grena (2010) developed a three-dimensional model based on the ray tracing recursive algorithm. In the following paper (Grena, 2011), he further discussed the efficiency gain of a PTC with an infrared-reflective film on the non-radiation part of the receiver. Jiang et al. (2010) established an optical model for two-stage PTCs using the spectral beam splitting method, which took into account the optical cone and the absorber diameter for the incident angle of  $0^\circ$ . Khanna et al. (2013, 2015) developed analytical expressions for both the circumferential and axial flux distribution on a bent absorber tube. Their optical models were relatively practical, and were verified by the following experimental results (Khanna et al., 2016).

In recent years, the Monte Carlo Ray Tracing (MCRT) method has been widely adopted to simulate the optical characteristics of concentrating solar collectors for its high efficiency and flexibility (Shuai et al., 2008; Wang et al., 2012, 2013; Yang et al., 2010). Cheng et al. (2013) developed a novel unified MCRT code for simulating typical concentrating solar collectors. In the later papers (Cheng et al., 2014a, 2014b), they investigated the concentrating characteristics of different PTCs based on MCRT. Many other researchers (Cheng et al., 2012; Hachicha et al., 2013; He et al., 2011; Wu et al., 2014) combined the MCRT with the Finite Volume Method (FVM) to study the photo-thermal conversion process of the PTC system.

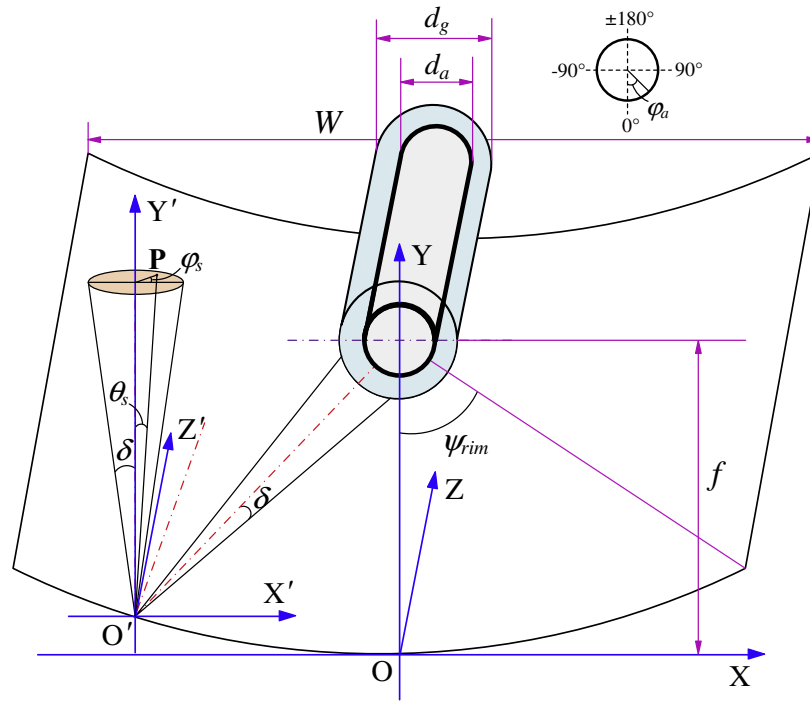
Although many researches on the optical performance of the PTC were conducted, seldom has literature been found which thoroughly discussed the effects of geometrical configuration on concentrating characteristics. In Refs. Cheng et al. (2014a, 2014b), only the sudden drop of the optical efficiency caused by rays escaping effect was theoretically explained. It did not give clear explanations of changes in some critical conditions, and never discussed the effects of these parameters on optical properties. In this paper, the flux distribution characteristics on the absorber of a PTC were

investigated in detail based on MCRT. And the effects of different geometrical parameters on the optical efficiency were further studied. Equations of several critical parameters were derived theoretically, and the variations of these parameters with different geometrical configurations were further displayed. Accordingly, the optical properties for different critical parameters were discussed. It was also proved that all the simulation results could be well explained by the theoretical analysis results.

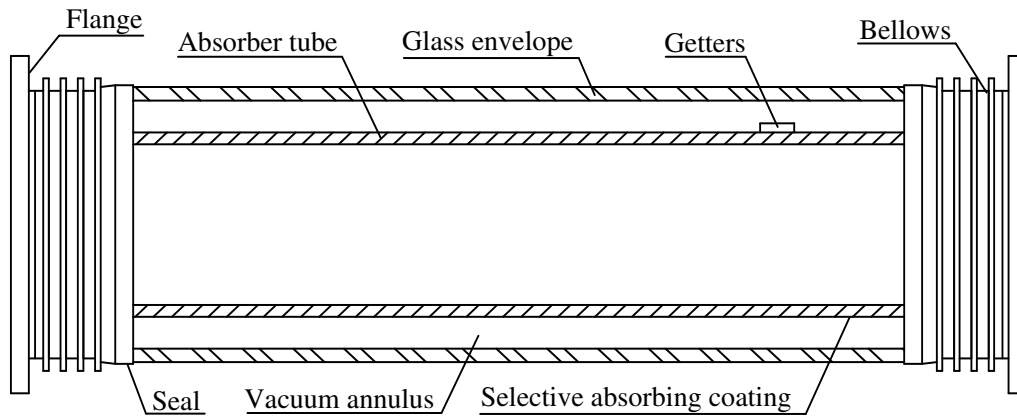
## 2. Model and methodology description

### 2.1. Physical model

The schematic diagram of a parabolic trough solar collector (PTC) is shown in Fig. 1(a). From the figure, it can be seen that a PTC module is mainly composed of a parabolic trough reflector and a receiver tube. Many important geometrical parameters are displayed in the figure, such as the aperture width ( $W$ ), the focal length ( $f$ ), the absorber tube outer diameter ( $d_a$ ), the glass envelope diameter ( $d_g$ ), the rim angle ( $\psi_{rim}$ ), and the radial angle of the sun ( $\delta$  signifies the finite size of the solar disk). The Cartesian coordinate system OXYZ used here is also established. The origin of coordinates (O) is the apex of parabola, X-Y plane contains the cross section of the parabolic trough, with Y axis passing through the vertex and the focus, and Z axis is through the vertex and parallel to the focal line. As is shown in Fig. 1(b), the receiver tube consists of a metal absorber tube with selective absorbing coatings on its outer surface and a glass envelope. The annulus between the metal absorber and glass envelope is kept vacuum to reduce heat loss and protect the coatings from oxidation. Metal bellows are used as the metal-glass joints to compensate the expansion difference between the metal and glass. Some other parts, such as getters and evacuation nozzle may also be used to maintain the vacuum state in the annulus.



(a) Schematic of a PTC module



(b) Schematic of the receiver tube

**Fig. 1.** Schematic diagram of the physical model of a PTC.

The SEGS LS-2 PTC module has been tested on the AZTRAK rotating test platform at Sandia National Laboratory (SNL) (Dudley et al., 1994), and detailed test data, which were widely used as the reference for other studies, were obtained. In this work,

the SEGS LS-2 PTC module is also adopted as the original physical model, whose specifications are shown in Table 1.

## 2.2. MCRT model

Monte Carlo Ray Tracing (MCRT) method combines the Monte Carlo Method (MCM), based on statistics and randomized trials, with the Ray Tracing Method (RTM), based on geometrical optics. First, it initializes the position, direction, energy of each ray on the aperture plane of the PTC by probability distribution functions. And then the optical behaviors, such as reflection, transmission, refraction, absorption, on each interface are determined by a series of uniformly distributed random numbers, and the propagating path of each ray in the PTC system is traced accordingly. At last, the intersection point position of each ray on the absorber surface is calculated and recorded. From the recorded data, the energy flux

**Table 1**  
Parameters of SEGS LS-2 PTC module.

Parameter	Value	Unit
$W$	5	m
$f$	1.84	m
$L_a$	7.8	m
$d_a$	0.07	m
$d_g$	0.115	m
$\alpha_a$	0.96	—
$\rho_r$	0.93	—
$\tau_g$	0.95	—

density on the absorber surface is determined, and some other optical performance can also be further obtained.

All the optical models used in this paper are based on several assumptions (ideal condition): (1) The brightness on the solar disk is uniform and the circumsolar ratio is viewed as zero. (2) The reflectivity, transmissivity and absorptivity are independent of the incident angle. (3) The effects of the refraction of glass envelope and the reflection of absorber tube are ignored. The present work will study in depth the optical performance of PTCs under conditions of zero incident angle, the schematic of which is shown in Fig. 1(a).

As Fig. 1(a) depicts, two Cartesian coordinate systems (OXYZ and O'X'Y'Z') are established. The coordinate of hitting point ( $x_0, y_0, z_0$ ) can be expressed by Eq. (1).

$$\begin{cases} x_0 = W \cdot \kappa_1 - W/2 \\ y_0 = \frac{x_0^2}{4f} \\ z_0 = L_a \cdot \kappa_2 \end{cases} \quad (1)$$

Assuming  $PO' = l'$ , the starting point (P) of a ray on the solar disk in coordinate system O'X'Y'Z' is given by Eq. (2).

$$\begin{cases} x' = l' \sin \theta_s \cos \varphi_s \\ y' = l' \cos \theta_s \\ z' = l' \sin \theta_s \sin \varphi_s \end{cases} \quad (2)$$

Thus, considering the symmetry of the solar disk, the unit direction vector of the incident ray in coordinate system O'X'Y'Z' can be expressed by Eq. (3).

$$\vec{S}' = (\sin \theta_s \cos \varphi_s, -\cos \theta_s, \sin \theta_s \sin \varphi_s) \quad (3)$$

The radial angle ( $\theta_s$ ) and the circumferential angle ( $\varphi_s$ ) of the starting point (P) on the solar disk are given by Eq. (4).

$$\begin{cases} \theta_s = \arctan(\sqrt{\kappa_3} \tan \delta) \\ \varphi_s = 2 \cdot \pi \cdot \kappa_4 \end{cases} \quad (4)$$

From Fig. 1(a), it can be clearly seen that the coordinate system O'X'Y'Z' can be realized simply through the translation of the coordinate system OXYZ. As we all know, the translation will not change a vector. Therefore, the unit direction vector ( $\vec{S}$ ) in coordinate system OXYZ is the same as that ( $\vec{S}'$ ) in coordinate O'X'Y'Z', which is given by Eq. (5).

$$\vec{S} = \vec{S}' \quad (5)$$

The equations of the parabolic reflector and the outer surface of the glass cover are expressed by Eqs. (6) and (7), respectively.

$$x^2 = 4fy \quad (6)$$

$$x^2 + (y - f)^2 = d_g^2/4 \quad (7)$$

The inner normal unit vector of them are  $\vec{n}_0$  and  $\vec{n}_1$ , and given by Eqs. (8) and (9), respectively.

$$\vec{n}_0 = \left( -\frac{x}{\sqrt{x^2 + 4f^2}}, \frac{2f}{\sqrt{x^2 + 4f^2}}, 0 \right) \quad (8)$$

$$\vec{n}_1 = \left( -\frac{2x}{d_g}, -\frac{2(y-f)}{d_g}, 0 \right) \quad (9)$$

If  $\vec{\lambda}$ ,  $\vec{n}$  and  $\vec{r}$  represent the unit incident ray vector, the normal unit vector, and the unit reflected ray vector of a surface (parabolic reflector or glass cover), the following equation can be obtained based on Fresnel law.

$$\vec{r} = \vec{\lambda} - 2 \cdot (\vec{\lambda} \cdot \vec{n}) \cdot \vec{n} \quad (10)$$

When a ray reaches a surface, an optical behavior (reflection, absorption or transmission) happens. The judgement of the optical behavior is made based on a uniformly generated random number. For example, when a ray reaches the surface of the reflector, a random number ( $\kappa_5$ ) will be generated, and used for comparing with the reflectivity ( $\rho_r$ ) of the reflector. If  $\kappa_5 \leq \rho_r$ , the ray is reflected, or it will be abandoned. Other optical behaviors, such as transmission and absorption, are judged by the same way. Corresponding random numbers ( $\kappa_6, \kappa_7$  and  $\kappa_8$ ) are also be generated and used. To be more clearly, the flowchart of the MCRT is shown in Fig. 2.

### 3. Parameter derivation and definition

Some important parameters will be used to analyze simulation results in the section of results and discussion. Thanks to the sun

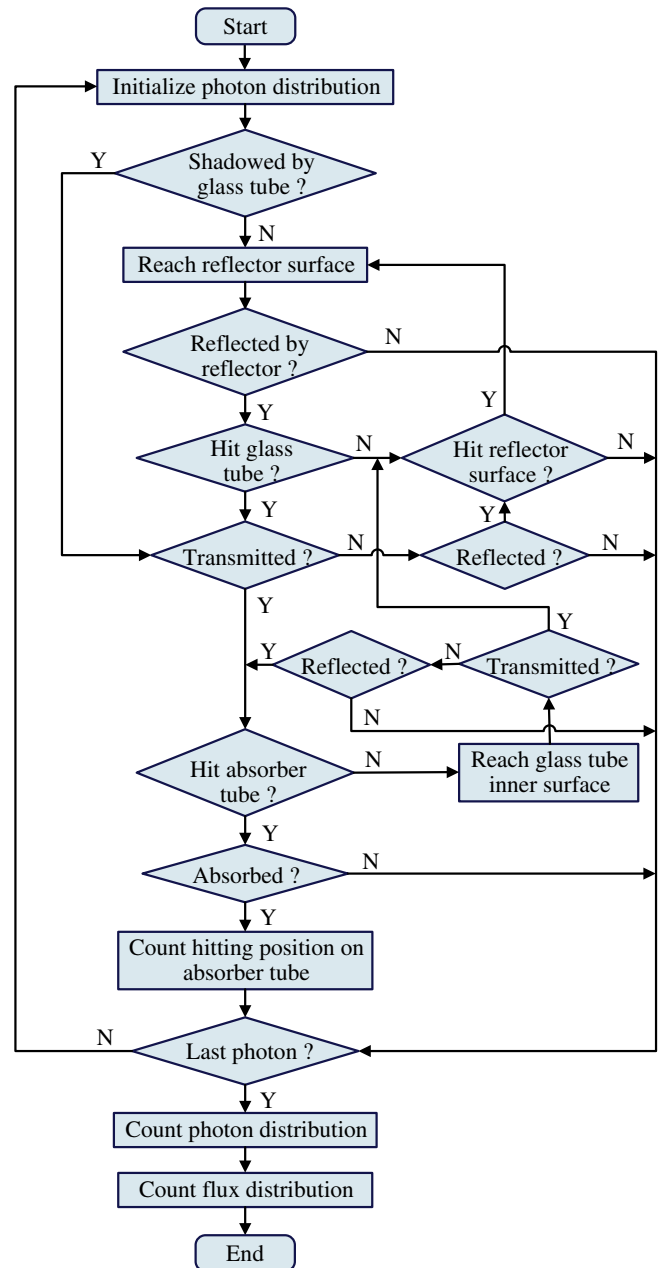


Fig. 2. The flowchart of MCRT.

size ( $\delta = 4.65 \text{ mrad}$ ), a reflected light cone will be formed, which greatly affects the optical performance (Jeter, 1986a, 1986b). Generally, the outer diameter of the absorber ( $d_a$ ) has to be larger than the diameter of the light cone in order to prevent rays escaping from around the absorber tube. The required minimum outer diameter of the absorber ( $d_{a, \text{re}}$ ) can be calculated by Eq. (11) (Cheng et al., 2014a, 2014b).

$$d_{a, \text{re}} = 2 \cdot \left( \frac{W^2}{16f} + f \right) \cdot \sin \delta \quad (11)$$

The rim angle ( $\psi_{\text{rim}}$ ) is the angle between the reflected rays from the reflector edge and Y axis (as shown in Fig. 1(a)), which is theoretically given by Eq. (12).

$$\psi_{\text{rim}} = \begin{cases} \arcsin \left( \frac{8(W/f)}{(W/f)^2 + 16} \right) & 0^\circ < \psi_{\text{rim}} \leq 90^\circ \\ 180 - \arcsin \left( \frac{8(W/f)}{(W/f)^2 + 16} \right) & 90^\circ < \psi_{\text{rim}} < 180^\circ \end{cases} \quad (12)$$

Generally, the upper side of the absorber tube absorbs the solar radiation directly, and the bottom side receives the concentrated solar beam from the reflector. Obviously, both the areas that receive concentrated beam and that receive directly incident rays change with different geometrical parameters of the PTC. The general concentrating process of the PTC is depicted in Fig. 3(a). We can see that the reflected beam from point A forms a focal shape  $\widehat{\text{BG}}$  on the absorber tube. According to the characteristics of the parabola, AC can be expressed by Eq. (13).

$$\text{AC} = \frac{x_A^2}{4f} + f \quad (13)$$

In  $\triangle \text{ABC}$ ,  $\angle \text{BCA}$  can be calculated by the law of sines and given by Eq. (14).

$$\phi = \angle \text{BCA} = \arcsin \left[ \left( \frac{x_A^2}{2fd_a} + \frac{2f}{d_a} \right) \cdot \sin \delta \right] - \delta \quad (14)$$

It can be easily seen that the arc  $\widehat{\text{BF}}$  will receives concentrated beam when the point of the reflected rays varies in the arc  $\widehat{\text{AO}}$ . Thus, the angle span that receives concentrated beam can be obtained when the point A is the edge of the parabola. Under this condition, the abscissa of point A is  $\pm W/2$ , and the position angle  $\psi$  is equal to the rim angle  $\psi_{\text{rim}}$ . Considering the symmetry of the parabola, the angle span that receives concentrated beam can be calculated by Eq. (15).

$$\Omega = 2 \cdot \left( \psi_{\text{rim}} + \arcsin \left[ \left( \frac{W^2}{8fd_a} + \frac{2f}{d_a} \right) \cdot \sin \delta \right] - \delta \right) \quad (15)$$

When the outer diameter of the absorber is smaller than the required diameter ( $d_a < d_{a, \text{re}}$ ), partial reflected beam will escape from around the absorber. As Fig. 3(b) shows,  $\text{AB}'$  is the outermost ray of the reflected light cone ( $\angle \text{B}'\text{AC} = \delta$ ), and AB is the reflected ray within the light cone, which is tangent to the absorber. From the figure, we can easily see that the reflected rays in  $\angle \text{B}'\text{AB}$  will escape from around the absorber. In  $\triangle \text{ABC}$ ,  $\angle \text{BCA}$  can be given by Eq. (16).

$$\phi = \angle \text{BCA} = 90 - (\angle \text{B}'\text{AC} - \angle \text{B}'\text{AB}) = 90 - (\delta - \angle \text{B}'\text{AB}) \quad (16)$$

$\angle \text{B}'\text{AB}$  is smaller than  $\delta$  ( $\delta = 4.65 \text{ mrad} = 0.27^\circ$ ) and thus, compared with 90, has little effect on the whole receiving angle. Eq. (16) can be concisely expressed as Eq. (17).

$$\phi = \angle \text{BCA} = 90 - \delta \quad (17)$$

As a result, the comprehensive expression of the angle span receiving concentrated beam ( $\Omega$ ) is presented as Eq. (18)

$$\Omega = \begin{cases} 2 \cdot \left( \psi_{\text{rim}} + \arcsin \left[ \left( \frac{W^2}{8fd_a} + \frac{2f}{d_a} \right) \cdot \sin \delta \right] - \delta \right) & d_a \geq d_{a, \text{re}} \\ 2 \cdot (\psi_{\text{rim}} + 90 - \delta) & d_a < d_{a, \text{re}} \end{cases} \quad (18)$$

If the focal length of the PTC ( $f$ ) is small enough or the outer diameter of the absorber tube ( $d_a$ ) is large enough, the bottom area of the absorber cannot receive any concentrated rays due to the shading effect of the absorber itself. From Fig. 3(a), we can see that the arc  $\widehat{\text{BG}}$  is the focal shape formed by the reflected beam from point A.  $\chi$  is the angle span that cannot receive reflected rays from point A. In  $\triangle \text{ACG}$  and  $\triangle \text{ACE}$ ,  $\angle \text{ACG}$  and  $\angle \text{ACE}$  can be calculated by Eqs. (19) and (20), respectively.

$$\angle \text{ACG} = \phi \quad (19)$$

$$\angle \text{ACE} = \psi = \arcsin \frac{\text{AE}}{\text{AC}} = \arcsin \left( \frac{|x_A|}{x_A^2/4f + f} \right) \quad (20)$$

Thus,  $\chi$  can be easily calculated by Eq. (21).

$$\chi = \angle \text{ACE} - \angle \text{ACG} = \psi - \phi \quad (21)$$

By Eqs. (14), (17), and (19)–(21), we can easily get the relationship between the angle span ( $\chi$ ) that cannot receive concentrated beam and the absolute value of the abscissa of point A ( $|x_A|$ ). If  $\chi$  stays greater than zero whichever point the reflected beam are from, an area that cannot receive any concentrated beam exists. As a result, the calculation equation (Eq. (18)) of the effective angle span ( $\Omega$ ) that receives concentrated beam should be modified as Eq. (22).

$$\Omega = \begin{cases} 2 \cdot \left( \psi_{\text{rim}} + \arcsin \left[ \left( \frac{W^2}{8fd_a} + \frac{2f}{d_a} \right) \cdot \sin \delta \right] - \delta \right) - 2 \cdot \chi & d_a \geq d_{a, \text{re}}, \chi > 0 \\ 2 \cdot (\psi_{\text{rim}} + 90 - \delta) - 2 \cdot \chi & d_a < d_{a, \text{re}}, \chi > 0 \end{cases} \quad (22)$$

A critical condition is shown in Fig. 3(c). The outermost ray (DA) of the incident optical cone is tangent to the absorber. The arc  $\widehat{\text{AO}}$  cannot receive any directly incident rays because of the shading effect of the absorber, and thus the arc  $\widehat{\text{GF}}$  cannot receive any reflected beam. It can be easily found from Fig. 3(c) that the coordinates of point D is  $(-\frac{d_a}{2} \cos \delta, -\frac{d_a}{2} \sin \delta + f)$ , and the direction vector of DA is  $(1, -\cot \delta)$ . Thus, the equation of line DA can be given by Eq. (23).

$$y = -\cot \delta \cdot \left( x + \frac{d_a}{2} \cos \delta \right) - \frac{d_a}{2} \sin \delta + f \quad (23)$$

By solving simultaneously Eqs. (6) and (23), the abscissa of point A is obtained, and expressed by Eq. (24).

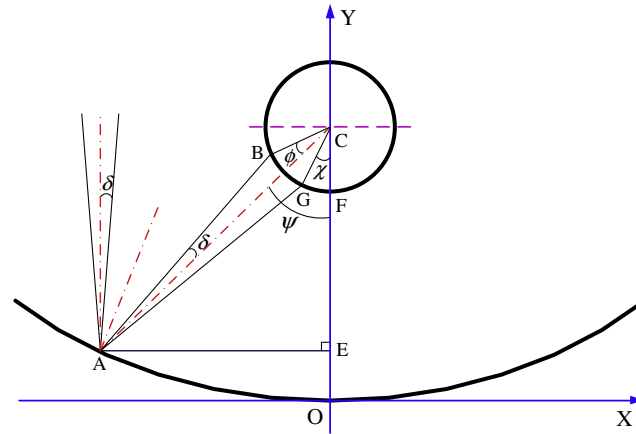
$$x_A = \sqrt{4f^2 \cot^2 \delta - 2f(d_a \cos \delta \cot \delta + d_a \sin \delta - 2f)} - 2f \cot \delta \quad (24)$$

The local concentration ratio ( $CL_i$ ) is defined as the ratio of local energy flux density ( $I_i$ ) to the effective solar radiation intensity ( $I_{\text{eff}}$ ) incident on the aperture, and expressed by Eq. (25). Note that the incident angle in this study is kept zero, and the effective solar radiation density ( $I_{\text{eff}}$ ) is equal to the direct normal solar radiation intensity ( $I_D$ ).

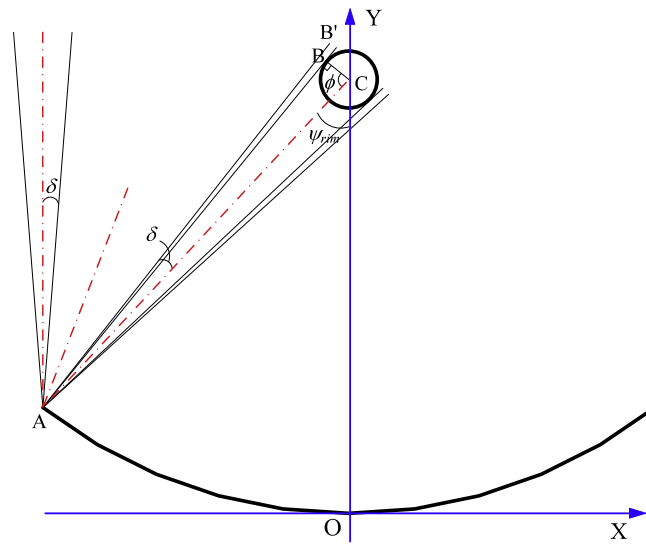
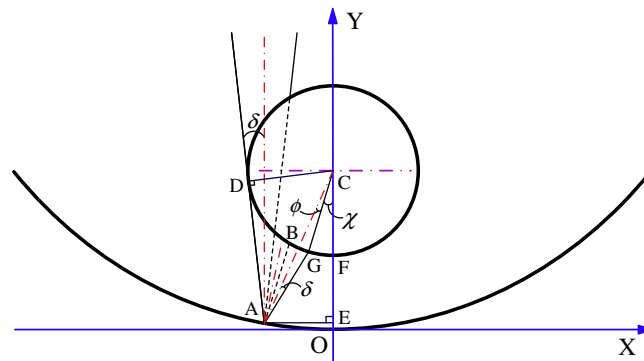
$$CL_i = \frac{I_i}{I_{\text{eff}}} \quad (25)$$

In order to analyze the characteristics of the energy flux density distribution in more detail, the average ( $CL_{\text{ave}}$ ) and the nonuniformity ( $\varepsilon$ ) of the energy distribution (Cheng et al., 2014a, 2014b) are further presented, the expression of which are given by Eq. (26) and Eq. (27) respectively.

$$CL_{\text{ave}} = \frac{\sum_{i=1}^{N_n} CL_i}{N_n} \quad (26)$$



(a) The general concentrating process

(b) The condition that  $d_a < d_{a,re}$ 

(c) The condition that the bottom of the absorber cannot receive concentrated beam

**Fig. 3.** Schematic of the angle span receiving concentrated beam ( $\delta$  is exaggerated for clarity).

$$\varepsilon = \frac{\sum_{i=1}^{N_n} |CL_i - CL_{ave}|}{N_n \cdot CL_{ave}} \quad (27)$$

The optical efficiency ( $\eta_o$ ) is defined as the ratio of absorbed energy to the total energy incident on the aperture, which can be calculated by Eq. (28).

$$\eta_o = \frac{\sum_{i=1}^{N_n} I_i \cdot A_i}{I_{eff} \cdot W \cdot L_a} \quad (28)$$

The intercept factor ( $\gamma$  is also a very important parameter for a PTC (Silverio et al., 2012), which is defined as the ratio of rays



intercepted by the absorber to the total rays incident on the aperture. The calculation formula is given by Eq. (29).

$$\gamma = \frac{\eta_o}{\rho_r \tau_g \alpha_a} \quad (29)$$

#### 4. Model validation

##### 4.1. Suitable grid configuration and number of rays

Considering the great nonuniformity of the energy flux density around the absorber tube, the number of grids ( $N_c$ ) in the circular direction of the absorber should be large enough. According to Ref. (Zhao et al., 2016), the results of 180 grid divisions were the best when the number of rays was less than  $10^8$ . Thus, 180 small sections around the absorber ( $N_c = 180$ ) are also adopted in this work. When the incident angle is zero, the energy flux density distribution in the length (axial) direction of the absorber is uniform. Thus, the absorber is viewed as a whole in the length direction ( $N_z = 1$ ).

In general, suitable number of rays should be determined based on both results' accuracy and computing time. According to Ref. Cheng et al. (2013), when  $5 \times 10^7$  rays are adopted, the simulation results are accurate enough. In order to further improve the accuracy of the results,  $8 \times 10^7$  rays ( $N_{ray} = 8 \times 10^7$ ) are adopted in current work.

##### 4.2. Model validation

The simulation results of the distribution of local concentration ratio (CL) around the absorber tube are compared with Jeter's results for the same geometry (Jeter, 1986a, 1986b), which are shown in Fig. 4. It can be clearly seen that the simulation results in this study agree very well with Jeter's results, verifying the correctness of the optical models used in this paper. As Fig. 4 presents, the distribution of local concentration ratio (CL) can be divided into four parts, which have been found and defined in Refs. (Cheng et al., 2014a, 2014b; He et al., 2011). The four parts are (I) the shelter region, (II) the energy flux increasing region, (III) the energy flux decreasing region and (IV) the direct insolation region. These four parts will change obviously with variations of the geometrical parameters of the PTC, which will be discussed in the following section.

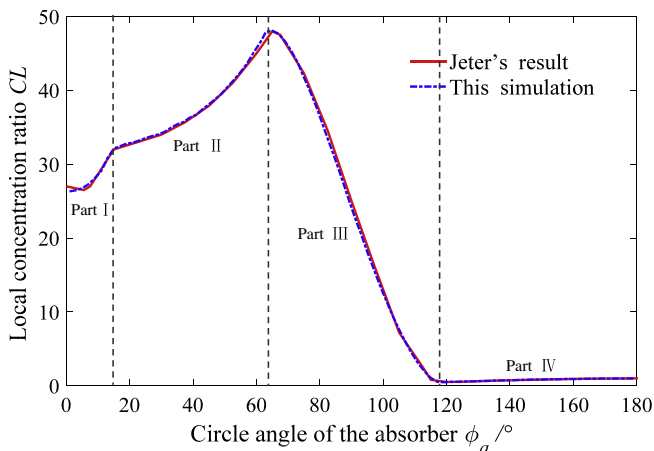


Fig. 4. Comparison of the distribution of the local concentration ratio (CL) between this work and Jeter's results.

#### 5. Results and discussion

The SEGS LS-2 PTC module, some important parameters of which are listed in Table 1, is used as the original physical model for this simulation. The direct normal solar radiation intensity ( $I_D$ ) is 1000 W/m<sup>2</sup>, and the radial angle ( $\delta$ ) of the sun is 4.65 mrad. The simulation results of optical performance of the PTC for a pill-box sun without degrading are discussed in detail in following parts, and corresponding theoretical analyses and explanations are also presented.

##### 5.1. Effects of aperture width

The variations of the distribution of local concentration ratio (CL) with aperture width ( $W$ ) for the SEGS LS-2 PTC module (other geometrical parameters remains constant) are shown in Fig. 5. Fig. 5(a) shows the results of the distribution of CL for  $W$  varying from 3 to 15 m. We can see from the figure that most distribution curves have the above mentioned four parts. The maximum of CL increases continuously with the increase of  $W$ , and the value of CL for  $\phi_a = 0^\circ$  remains constant at about 41. The angle span of the shelter region (part I) remains unchanged at about  $15^\circ$ . Nevertheless, both the energy flux increasing region (part II) and the energy flux decreasing region (part III) increase with increasing  $W$ , reducing the direct insolation region (part IV). The angle, which can be calculated by  $\phi + \psi_{rim}$ , corresponding to the minimum of CL in part III increases with the increase of  $W$ . When  $W$  reaches a certain degree (about 12 m), part IV disappears. Fig. 6 shows the theoretical results of different calculated angles for different aperture width ( $W$ ). From Fig. 6, it can be seen that the effective angle ( $\Omega$ ) receiving concentrated beam increases constantly with the increase of  $W$ , and completely coincides with  $2 \times (\phi + \psi_{rim})$  when  $W$  is less than 12 m, and reaches the maximum value of  $360^\circ$  afterwards. When  $2 \times (\phi + \psi_{rim})$  is  $180^\circ$  or  $360^\circ$ , the  $W$  is 5 m and 12 m, respectively. That means when  $W$  is less than 5 m, the angle span from  $\phi + \psi_{rim}$  to  $90^\circ$  (also from  $-90^\circ$  to  $-(\phi + \psi_{rim})$ ) cannot receive any rays, and the entire absorber tube periphery will receive concentrated beam with  $W$  above 12 m. The same characteristics are shown in Fig. 5(a). The value of  $\phi_a$  corresponding to the minimum CL is  $90^\circ$  (and  $-90^\circ$ ) with  $W = 5$  m and decreases with  $W$  less than 5 m. The CL in the angle span from  $\phi_a$  to  $90^\circ$  is zero when  $W$  is less than 5 m. When  $W$  is larger than 12 m, the angle spans of part I, part II and part III cover the whole circumference of the absorber tube, and part IV disappears. All the analyses above prove that the simulation results accord very well with the theoretical results. The results for some small values of  $W$  are further studied and depicted in Fig. 5(b). It can be clearly observed that part II becomes smaller and smaller when  $W$  is less than 2 m, and disappears totally with  $W$  less than 0.92 m. When  $W$  is smaller than 0.92 m, the value of CL for  $\phi_a = 0^\circ$  is smaller than 41. To be more clearly, a partially enlarged view is shown in Fig. 5(c). It can be seen that when  $W = 0.92$  m, the only peak value of the CL is 41 corresponding to  $\phi_a$  of  $0^\circ$ . All these phenomena can be explained by the theoretical results shown in Fig. 7. It can be easily seen from Fig. 7 that  $\chi$  increases with the increase of the absolute value of the abscissas of point A (using absolute value because of the symmetry of the parabola). When  $|x_A|$  is less than 0.46,  $\chi$  is negative, which indicates that the reflected cone from any points that are in the range between 0 and 0.46 can cover the bottom of the absorber ( $\phi_a = 0^\circ$ ). Besides, only is  $|x_A|$  less than 0.46, the reflected rays can reach the bottom of absorber tube. Consequently, the value of CL for  $\phi_a = 0^\circ$  stays constant with  $W$  ( $W = 2|x_A|$ ) larger than 0.92 m. When  $W$  is smaller than 0.92 m, the value of CL for  $\phi_a = 0^\circ$  will be smaller than 41 due to smaller reflection area of the parabolic reflector.

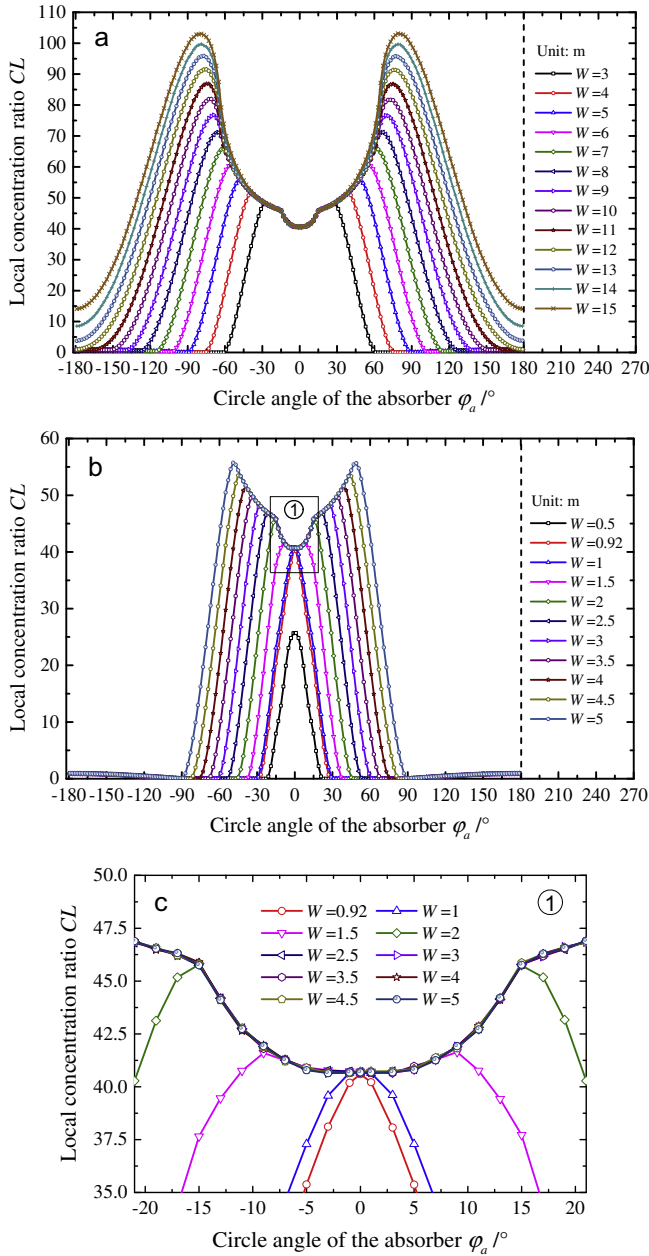


**Fig. 5.** Effects of aperture width (W) on the distribution of local concentration ratio (CL).

The variations of the optical efficiency ( $\eta_o$ ) and the intercept factor ( $\gamma$ ) for different W are shown in Fig. 8. From the figure, we can find that  $\eta_o$  almost stays constant at a high value of 83.8% when W is less than 12.93 m, and drops significantly afterwards. The same variation trend is also shown for  $\gamma$ , which means that there are rays escaping from the PTC system when W is larger than 12.93 m. From the theoretical results presented in Fig. 9, we can easily find the reason for this variation trend. As Fig. 9 shows, both the rim angle ( $\psi_{rim}$ ) and the required absorber diameter ( $d_{a, re}$ ) increase with increasing aperture width (W). It can be easily observed that when W is larger than 12.93 m,  $d_{a, re}$  will be larger than the absorber diameter ( $d_a = 0.07$  m), causing escaping of partial reflected rays from around the absorber. In this case, the absorber is just an interception of the reflected light cone, and the rays escaping has the dominating effect on the optical performance. Fig. 10 shows the variations of the maximum and the average local

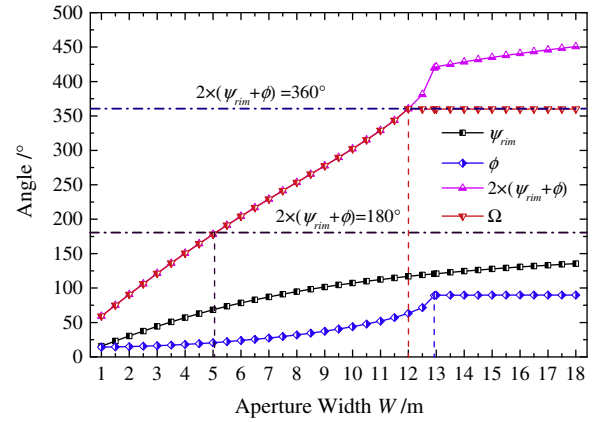


**Fig. 6.** Theoretical results of different calculated angles for different aperture width (W).

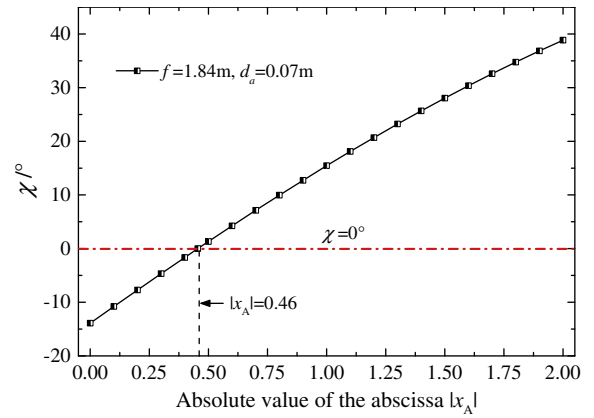


**Fig. 7.** Variation of  $\chi$  with the absolute value of abscissa of point A ( $|x_A|$ ).

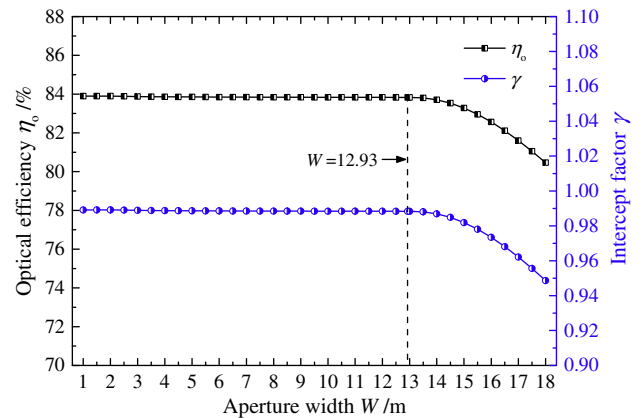


**Fig. 8.** Effects of aperture width (W) on optical efficiency ( $\eta_o$ ) and intercept factor ( $\gamma$ ).

concentration ratio ( $CL_{max}/CL_{ave}$ ) and the nonuniformity of the energy flux density distribution ( $\varepsilon$ ) with aperture width (W). From the figure, we can see that both the  $CL_{max}$  and  $CL_{ave}$  increase with the increase of W, whereas the variation trend of  $\varepsilon$  is inverse. The possible reason can also be found in Fig. 6. It can be observed that the effective angle span ( $\Omega$ ) receiving concentrated beam increases with the increase of W, which means the concentrated beam are distributed at a larger angle span, causing smaller nonuniformity ( $\varepsilon$ ). From the analyses above, the simulation results are well



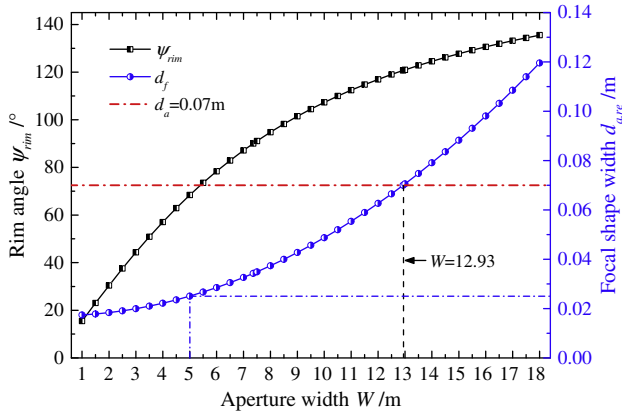
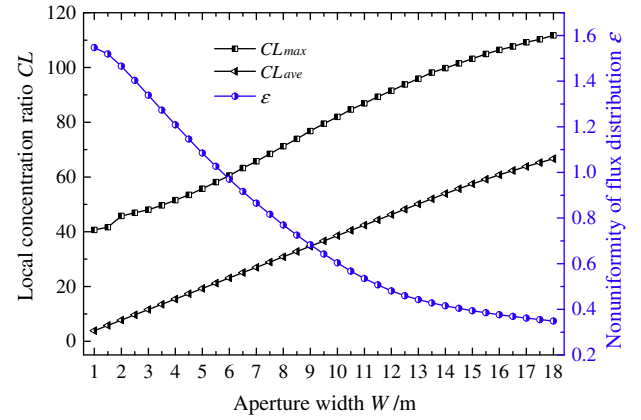


**Fig. 9.** Variations of the rim angle ( $\psi_{rim}$ ) and the required absorber diameter ( $d_{a,rc}$ ) with aperture width ( $W$ ).

validated by the theoretical results, demonstrating that the optical models used in this work are reliable and accurate.

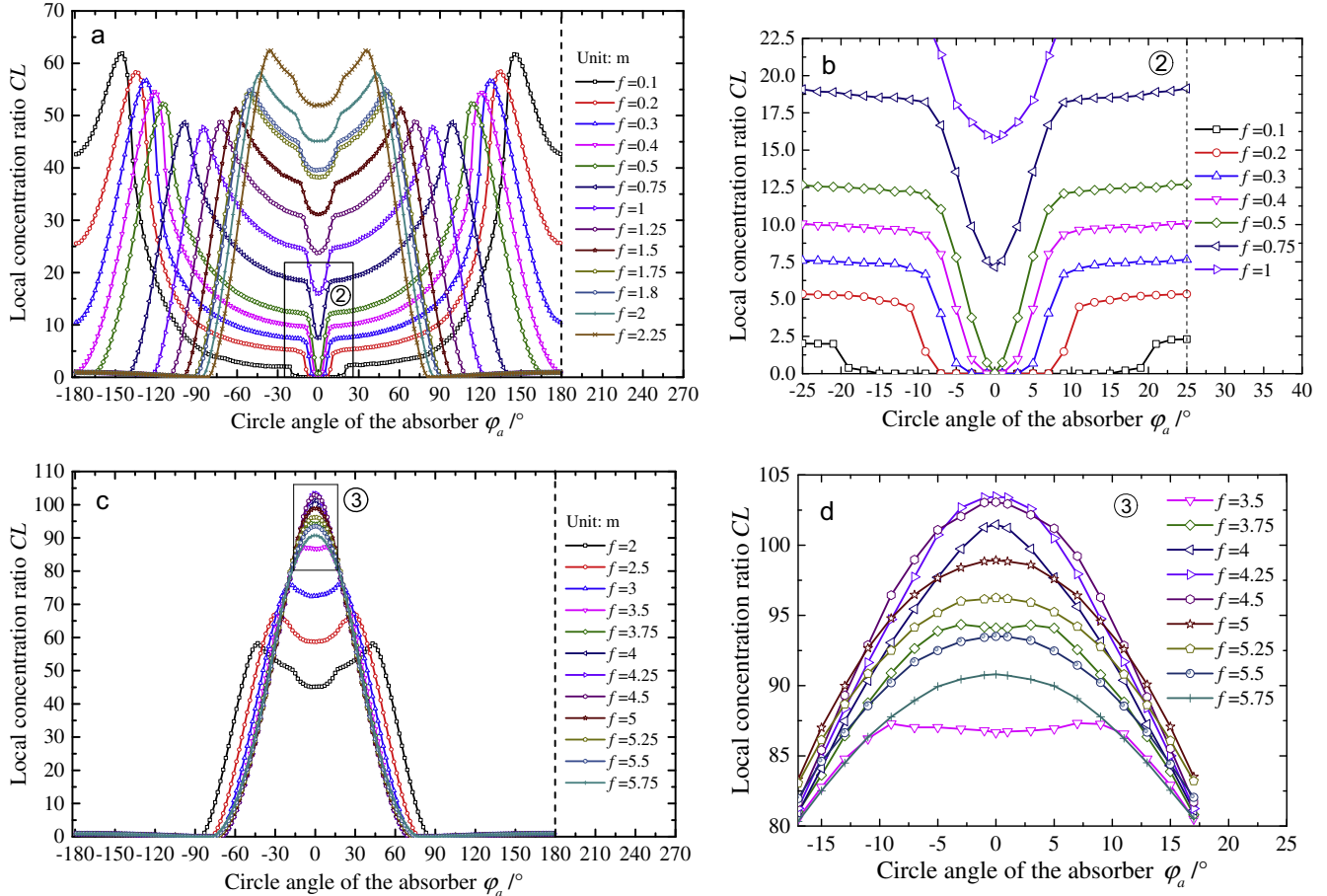
### 5.2. Effects of focal length

Fig. 11 shows the effects of the focal length ( $f$ ) on the distribution of CL for the SEGS LS-2 PTC module (other geometrical parameters stays constant). From Fig. 11(a), we can see that part II decreases obviously with increasing  $f$ , while part IV increases. It can also be found that when  $f$  is smaller than a certain degree



**Fig. 10.** Variations of the maximum and the average local concentration ratio ( $CL_{max}$ ,  $CL_{ave}$ ) and the nonuniformity of the energy flux density distribution ( $\epsilon$ ) with the aperture width ( $W$ ).

(about 0.5 m), an area with extremely low (almost zero) CL appears before part I, and part IV disappears with further decrease of  $f$  (smaller than 0.4 m). To be more clearly, a partially enlarged view is shown in Fig. 11(b). We can obviously see that the area with extremely low CL exists when  $f$  is less than 0.5 m, and the smaller  $f$  is, the larger this area is. The results for a series of larger values of  $f$  are depicted in Fig. 11(c). It can be seen that both part I and part II disappear when  $f$  is larger than 4 m, and the only peak value of CL is obtained at  $\phi_a = 0^\circ$ . To be more clearly, another partially enlarged view is shown in Fig. 11(d). From the figure, we can easily see that



**Fig. 11.** Effects of focal length ( $f$ ) on the distribution of local concentration ratio ( $CL$ ).

when  $f$  is larger than 4 m, only one peak value of  $CL$  exists at the position of  $\varphi_a = 0^\circ$ . All the simulation results presented above can be accounted for by the theoretical results shown in Figs. 12–14. Given that the aperture width of the adopted PTC module is 5 m (shown in Table 1), the maximum of the absolute value of the abscissa of point A ( $|x_A|$ ) is 2.5 m. It can be seen from Fig. 12 that  $\chi$  increases with the increase of  $|x_A|$ . When  $f$  is larger than 4 m,  $\chi$  is smaller than zero for any  $|x_A|$ , which indicates that the bottom of the absorber ( $\varphi_a = 0^\circ$ ) can receive reflected beam from any point of the reflector in this case. Thus, the only peak value of  $CL$  will always appear at the bottom of the absorber when  $f$  is more than 4 m. From Fig. 12, we can also find that the smaller  $|x_A|$  is, the smaller  $\chi$  is, and the minimum of  $\chi$  increases with the decrease of  $f$ . More detailed results are shown in Fig. 13.  $|x_{A\min}|$  is the minimum of the absolute value of the abscissa of point A, which represents the minimum value of the point that can receive directly solar rays incident on the reflector (shown in Fig. 3(c)). It can be observed that when  $f$  is less than 7.5 m, both  $\chi$  and  $|x_{A\min}|$  decrease with the increase of  $f$ . Afterwards,  $\chi$  almost keeps constant at  $-90^\circ$ , and  $|x_{A\min}|$  increases with further increasing  $f$ . When  $f$  is smaller than 0.5 m,  $\chi$  is larger than zero, which means that there is an area (the area with extremely low  $CL$  in Fig. 11(a)) at the absorber bottom that cannot receive any reflected rays from the reflector. We can also see that when  $f$  is smaller than 7.5,  $|x_{A\min}|$  remains positive and decreasing, indicating that there is

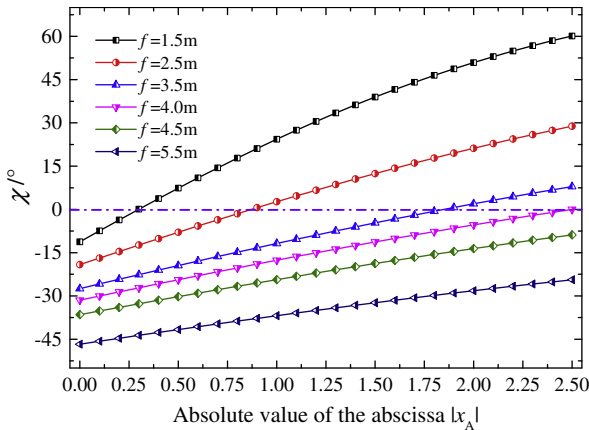


Fig. 12. Variation of  $\chi$  with the absolute value of abscissa of point A for different focal length ( $f$ ).

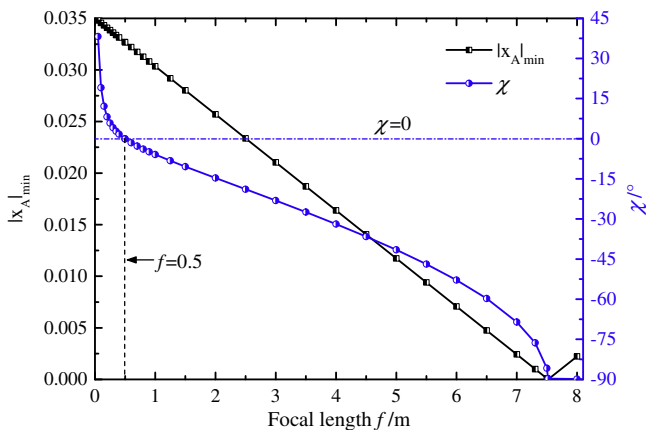


Fig. 13. Variations of the minimum absolute value of abscissa of point A ( $|x_{A\min}|$ ) and  $\chi$  with the focal length ( $f$ ).

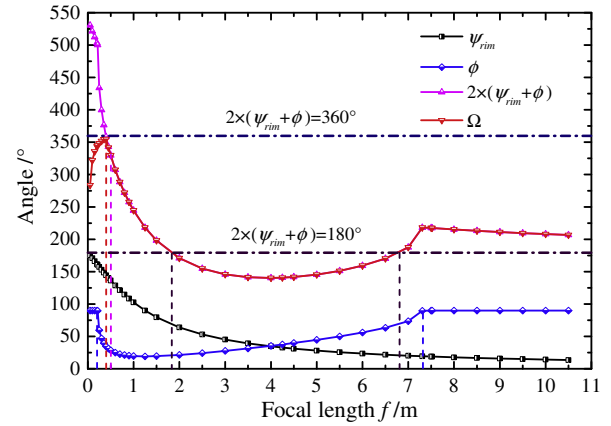


Fig. 14. Theoretical results of different calculated angles for different focal length ( $f$ ).

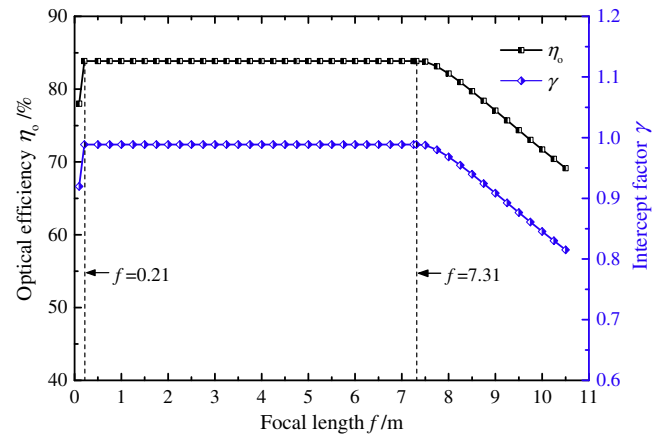
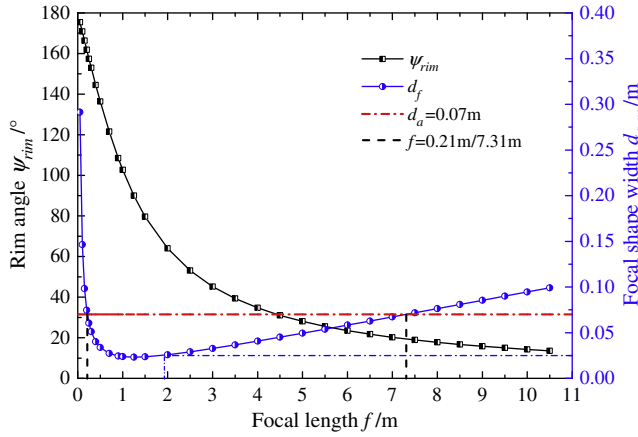


Fig. 15. Effects of focal length ( $f$ ) on optical efficiency ( $\eta_o$ ) and intercept factor ( $\gamma$ ).

an area on the parabolic reflector that cannot receive any directly incident solar rays. In practice, there is a small gap at the vertex of the parabolic reflector to install the bracket. Therefore, if half of the width of the gap is smaller than  $|x_{A\min}|$ , all the incident rays can be reflected by the reflector, otherwise some rays will escape from the gap, causing optical loss. Fig. 14 depicts the theoretical results of different calculated angles for different focal length ( $f$ ). As the figure shows, when  $f$  is smaller than 0.4 m,  $2 \times (\phi + \psi_{rim})$  is larger than  $360^\circ$ , which indicates that even the top ( $\varphi_a = 180^\circ$ ) of the absorber tube can receive concentrated beam, causing disappearance of part IV.

Fig. 15 shows the variations of  $\eta_o$  and  $\gamma$  with  $f$ . It can be clearly seen that both  $\eta_o$  and  $\gamma$  are kept almost constant at a high value when  $f$  varies from 0.21 m to 7.31 m. Whereas, a rapid drop appears when  $f$  is smaller than 0.21 m or larger than 7.31 m. The main reason can be found in Fig. 16, which presents the variations of  $\psi_{rim}$  and  $d_{a,re}$  with  $f$ . From the figure, we can see that  $\psi_{rim}$  decreases continuously, and  $d_{a,re}$  decreases sharply and then increases gradually with the increase of  $f$ . When  $f$  is smaller than 0.21 m or larger than 7.31 m,  $d_{a,re}$  is larger than  $d_a$  ( $d_a = 0.07$  m), causing rays escaping. Consequently,  $\eta_o$  is weakened greatly because of the rays escaping effect. Fig. 17 depicts the variations of  $CL_{max}$ ,  $CL_{ave}$  and  $\varepsilon$  with  $f$ . When  $f$  is less than 0.21 m or larger than 7.31 m,  $CL_{ave}$  decreases because of rays escaping.  $CL_{max}$  decreases first and then increases to the peak value at  $f = 4.25$  m, and drops afterwards with increasing  $f$ . The variation trend of  $\varepsilon$  is similar to that of  $CL_{max}$ . The minimum of  $\varepsilon$  appears for  $f = 0.5$  m, whereas



**Fig. 16.** Variations of the rim angle ( $\psi_{rim}$ ) and the required absorber diameter ( $d_{a,req}$ ) with focal length ( $f$ ).

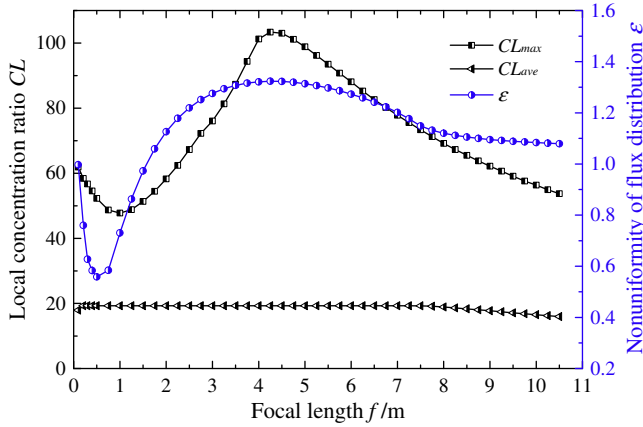
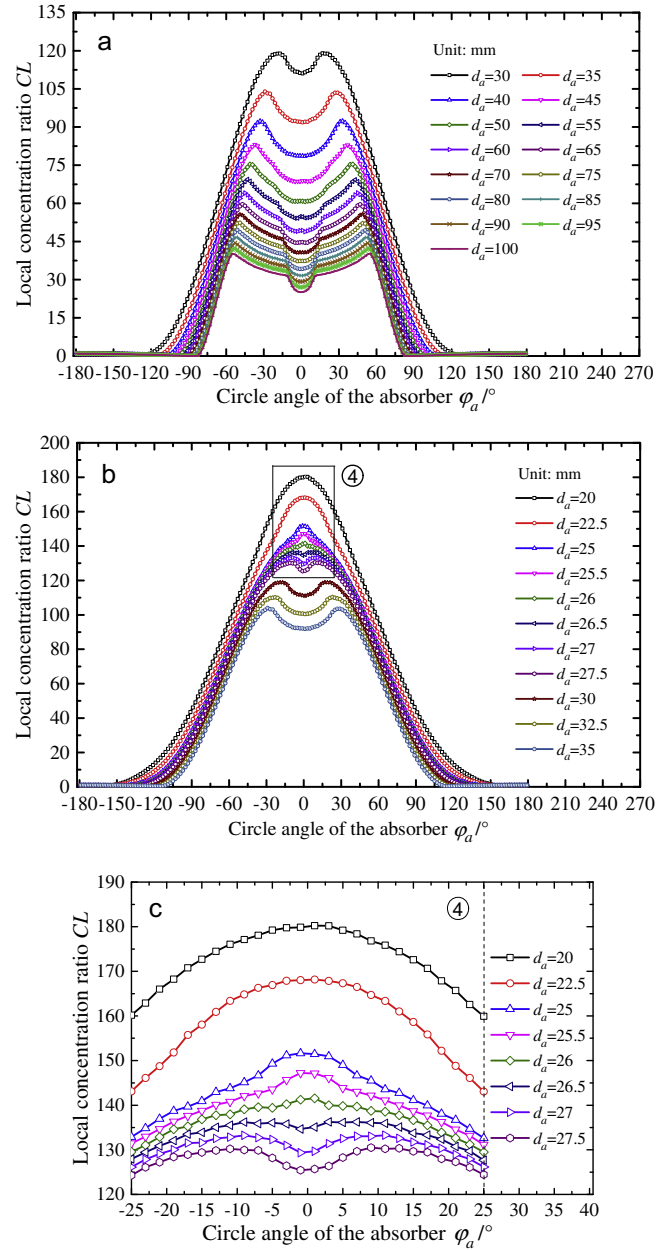


**Fig. 17.** Variations of the maximum and the average local concentration ratio ( $CL_{max}$ ,  $CL_{ave}$ ) and the nonuniformity of the energy flux density distribution ( $\varepsilon$ ) with the focal length ( $f$ ).

the minimum of  $CL_{max}$  appears for  $f = 1$  m. The possible reason may be found in Fig. 14. When  $f$  is about 0.5 m, the effective angle span ( $\Omega$ ) receiving concentrated beam is almost at the maximum value, which indicates that the concentrated beam is distributed at a large angle span, causing small nonuniformity ( $\varepsilon$ ). It can also be found in Fig. 17 that when  $f = 4.25$  m,  $\varepsilon$  reaches the maximum value and then decreases constantly. From Fig. 14, it is clearly seen that when  $f = 4.25$  m, the effective angle span ( $\Omega$ ) receiving concentrated beam is at the minimum value, which means the concentrated rays are distributed at the smallest angle span, leading to the largest nonuniformity ( $\varepsilon$ ).

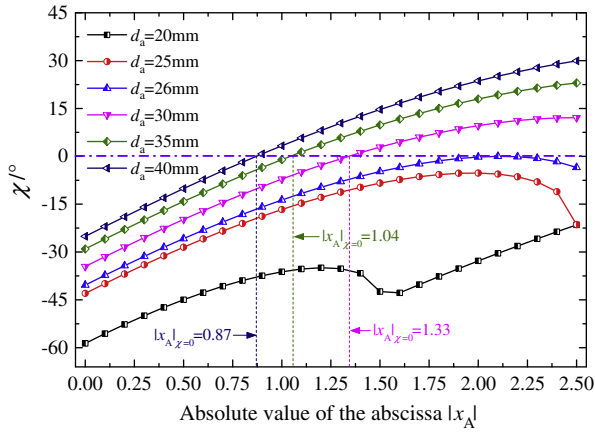
### 5.3. Effects of absorber diameter

Fig. 18 shows the effects of the absorber diameter ( $d_a$ ) on the distribution of  $CL$  for the SEGS LS-2 PTC module (other geometrical parameters stays constant). From Fig. 18(a), It can be found that the angular range of both part II and part IV increase with the increase of  $d_a$ , while part III decreases. When  $d_a$  is small to a certain extent (about 50 mm), part I disappears. The results for a series of smaller values of  $d_a$  are depicted in Fig. 18(b). It can be seen that both part I and part II disappear when  $d_a$  is smaller than a certain value (about 26 mm), and the only peak value of  $CL$  is obtained at  $\varphi_a = 0^\circ$ . For greater clarity, a partially enlarged view is shown in



**Fig. 18.** Effects of absorber diameter ( $d_a$ ) on the distribution of local concentration ratio ( $CL$ ).

Fig. 18(c). From the figure, we can easily find that when  $d_a$  is smaller than 26 mm, only one peak value of  $CL$  exists at the position of  $\varphi_a = 0^\circ$ . The possible reason can be found from theoretical results shown in Fig. 19. It can be clearly observed that when  $d_a$  is smaller than 26 mm, the maximum of  $\chi$  is smaller than zero for any  $|x_A|$ , which indicates that the bottom of the absorber ( $\varphi_a = 0^\circ$ ) can receive all the reflected beam from any point of the reflector. Therefore, the only peak value of  $CL$  will always appear at the bottom of the absorber ( $\varphi_a = 0^\circ$ ) in this case. From Fig. 19, we can also found that when  $d_a$  is larger than 26 mm,  $\chi$  will be greater than zero for  $|x_A|$  larger than a certain value. Assuming that the value of  $|x_A|$  corresponding to  $\chi = 0^\circ$  is  $|x_A|_{\chi=0}$ . It is clearly seen that  $|x_A|_{\chi=0}$  decreases with the increase of  $d_a$ . This indicates that the larger the absorber diameter ( $d_a$ ) is, the less the bottom ( $\varphi_a = 0^\circ$ ) of the absorber receive reflected beam, which will lead to smaller  $CL$  at  $\varphi_a = 0^\circ$ . Obviously, Fig. 18 shows that the value of  $CL$  for



**Fig. 19.** Variation of  $\chi$  with the absolute value of abscissa of point A ( $|x_A|_{\min}$ ) for different absorber diameter ( $d_a$ ).

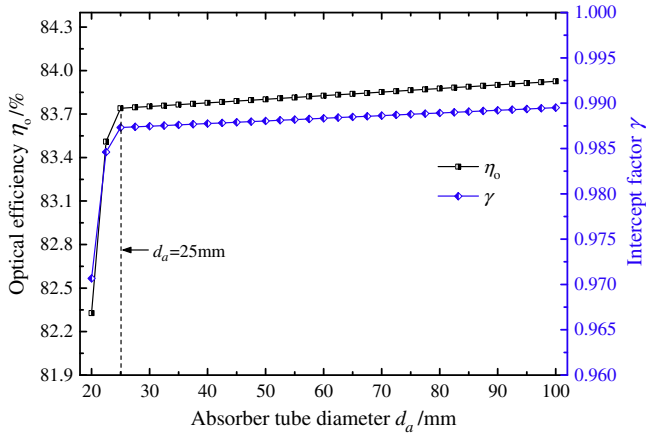


**Fig. 20.** Effects of absorber diameter ( $d_a$ ) on optical efficiency ( $\eta_o$ ) and intercept factor ( $\gamma$ ).

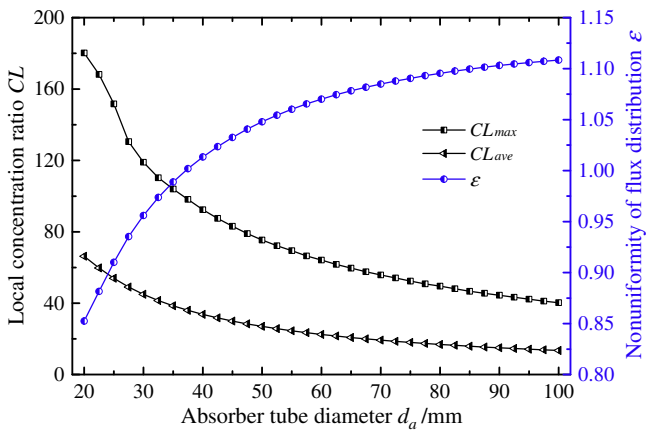


**Fig. 21.** Variations of the maximum and the average local concentration ratio ( $CL_{\max}$ ,  $CL_{ave}$ ) and the nonuniformity of the energy flux density distribution ( $\epsilon$ ) with the absorber diameter ( $d_a$ ).

$\varphi_a = 0^\circ$  decreases continuously with the increase of  $d_a$ , which is in conformity with the above theoretical analysis results.

Fig. 20 shows the variations of  $\eta_o$  and  $\gamma$  with  $d_a$ . It can be clearly seen that both  $\eta_o$  and  $\gamma$  increase gradually when  $d_a$  is more than 25 mm. This is because the larger the absorber diameter ( $d_a$ ) is,

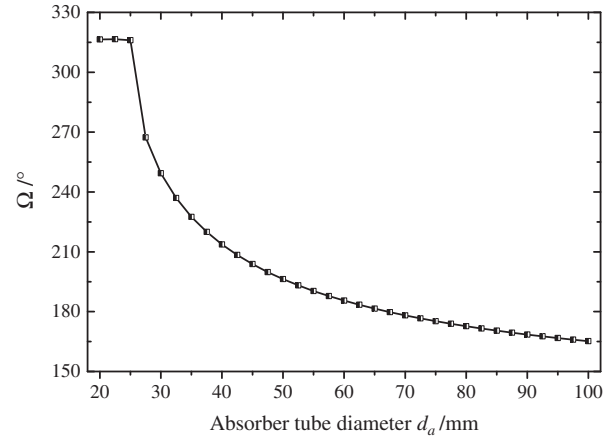


**Fig. 22.** Variation of the effective angle span ( $\Omega$ ) receiving concentrated beam with absorber diameter ( $d_a$ ).

the smaller the annular space will be, and thus the less the reflected rays can escape from it. Also, the absorber will receive more directly incident rays when the absorber diameter increases. However, both  $\eta_o$  and  $\gamma$  decrease sharply for  $d_a$  less than 25 mm. This can also be explained by the rays escaping effect. As Figs. 9 and 16 show (the blue dash dot line), the required diameter  $d_{a, re}$  for the adopted PTC module ( $W = 5$  m and  $f = 1.84$  m) is 25 mm. So, when  $d_a$  is less than 25 mm, rays escaping is the dominating factor weakening the optical efficiency ( $\eta_o$ ). Fig. 21 shows the variations of  $CL_{\max}$ ,  $CL_{ave}$  and  $\epsilon$  with  $d_a$ . From the figure, we can see that both the  $CL_{\max}$  and  $CL_{ave}$  decrease with the increase of  $d_a$ , whereas the variation trend of  $\epsilon$  is inverse. The possible reason can be found in Fig. 22. We can observe that the effective angle span ( $\Omega$ ) receiving concentrated beam decreases with the increase of  $d_a$ , which demonstrates that the concentrated beam are distributed at a smaller angle span, causing larger nonuniformity ( $\epsilon$ ).

## 6. Conclusions

This paper presented the detailed findings of the study on the optical performance of a PTC based on MCRT and theoretical analysis. The MCRT optical models were established, and the effects of different geometrical parameters on the optical performance were investigated in detail. Formulas of several critical parameters to calculate the angle span of each flux distribution region were derived theoretically, and the variations of those parameters with different geometrical configurations were further displayed. Accordingly, the optical properties for different critical parameters were discussed. It was proved that all the simulation results could be explained very well by the theoretical analysis results. All the findings in this paper are the foundation for further research on the optical-to-thermal energy conversion in the PTC system, and are also of great significance for designing and optimizing PTC's structure. Several conclusions can be drawn as follows.

1. Geometrical parameters, including aperture width, focal length and absorber diameter, have great effects on the optical performance of the PTC. The distribution of local concentration ratio around the absorber tube varies greatly with different geometrical configurations and for some special parameter conditions, it cannot be divided into four parts, unlike the findings in previous references.
2. Related critical parameters are derived theoretically, and the variation of these parameters with different PTC's geometrical configurations are discussed. The effects of these critical



parameters on optical performance are analyzed. Simulation results, especially some special properties such as the rays escaping effect, the shading effects, the variation of the angle span of each flux distribution region and the nonuniformity of the flux distribution, can be well predicted and explained by theoretical results for any geometrical configuration.

3. The size relationship between the reflected light cone and the absorber diameter is an important factor that affects the optical efficiency significantly. In practice, the absorber diameter has to be larger than the spot size of the reflected light cone on the absorber to avoid rays escaping which can cause great optical loss.

Actually, various optical errors, such as tracking error, installation error, surface error etc. and the real sunshape (non-uniform distribution) affect the performance of the PTC obviously under realistic conditions. Thus, the comprehensive characteristics obtained under realistic conditions should also be significant. Corresponding investigations on practical operation performance are currently conducted by us, and some meaningful findings have been obtained and will be presented in the next paper.

## Acknowledgements

The authors acknowledge the financial supports from the China Postdoctoral Science Foundation funded project (No. 2016T90297).

## References

- Buie, D., Monger, A.G., Dey, C.J., 2003a. Sunshape distributions for terrestrial solar simulations. *Sol. Energy* 74, 113–122.
- Buie, D., Dey, C.J., Bosi, S., 2003b. The effective size of the solar cone for solar concentrating systems. *Sol. Energy* 74, 417–427.
- Burkhard, D.G., Shealy, D.L., Sexl, R.U., 1973. Specular reflection of heat radiation from an arbitrary reflection of heat radiation from an arbitrary receiver surface. *Int. J. Heat Mass Transfer* 16, 271–280.
- Cheng, Z.D., He, Y.L., Xiao, J., Tao, Y.B., et al., 2010. Three-dimensional numerical study of heat transfer characteristics in the receiver tube of parabolic trough solar collector. *Int. Commun. Heat Mass Transfer* 37, 782–787.
- Cheng, Z.D., He, Y.L., Cui, F.Q., Xu, R.J., et al., 2012. Numerical simulation of a parabolic trough solar collector with nonuniform solar flux conditions by coupling FVM and MCRT method. *Sol. Energy* 86, 1770–1784.
- Cheng, Z.D., He, Y.L., Cui, F.Q., 2013. A new modelling method and unified code with MCRT for concentrating solar collectors and its applications. *Appl. Energy* 101, 686–698.
- Cheng, Z.D., He, Y.L., Wang, K., Du, B.C., et al., 2014a. A detailed parameter study on the comprehensive characteristics and performance of a parabolic trough solar collector system. *Appl. Therm. Eng.* 63, 278–289.
- Cheng, Z.D., He, Y.L., Cui, F.Q., Du, B.C., et al., 2014b. Comparative and sensitive analysis for parabolic trough solar collectors with a detailed Monte Carlo ray-tracing optical model. *Appl. Energy* 115, 559–572.
- Daly, J.C., 1979. Solar concentrator flux distributions using backward ray tracing. *Appl. Opt.* 18, 2696–2699.
- Dudley, V., Kolb, G., Sloan, M., Kearney, D., 1994. SEGS LS2 solar collector – test results. Report of Sandia National Laboratories, SANDIA 94–1884, USA.
- Duran, J.C., Nicolas, R.O., 1984. Development and application of a two-dimensional optical analysis of non-perfect cylindrical concentrators. *Sol. Energy* 34, 257–269.
- Evans, D.L., 1977. On the performance of cylindrical parabolic solar concentrators with flat absorbers. *Sol. Energy* 19, 379–385.
- Fernandez, G.A., Zarza, E., Valenzuela, L., Perez, M., 2010. Parabolic-trough solar collectors and their applications. *Renew. Sustain. Energy Rev.* 14, 1695–1721.
- Geyer, M., 2007. International market introduction of concentrated solar power policies and benefits. In: *Proceedings of ISES Solar World Congress 2007: Solar Energy and Human Settlement*, vol. 1, Beijing, China, September 18–21, pp. 75–82.
- Grena, R., 2010. Optical simulation of a parabolic solar trough collector. *Int. J. Sustain. Energy* 29, 19–36.
- Grena, R., 2011. Efficiency Gain of a solar trough collector due to an ir-reflective film on the non-irradiated part of the receiver. *Int. J. Green Energy* 8, 715–733.
- Hachicha, A.A., Rodríguez, I., Capdevila, R., Oliva, A., 2013. Heat transfer analysis and numerical simulation of a parabolic trough solar collector. *Appl. Energy* 111, 581–592.
- He, Y.L., Xiao, J., Cheng, Z.D., Tao, Y.B., 2011. A MCRT and FVM coupled simulation method for energy conversion process in parabolic trough solar collector. *Renew. Energy* 36, 976–985.
- He, Y.L., Cheng, Z.D., Cui, F.Q., Li, Z.Y., 2012. Numerical investigations on a pressurized volumetric receiver: solar concentrating and collecting modelling. *Renew. Energy* 44, 368–379.
- Huang, W.D., Hu, P., Chen, Z.S., 2012. Performance simulation of a parabolic trough solar collector. *Sol. Energy* 86, 746–755.
- Jebasingh, V.K., Joselin-Herbert, G.M., 2016. A review of solar parabolic trough collector. *Renew. Sustain. Energy Rev.* 54, 1085–1091.
- Jeter, S.M., 1986a. The distribution of concentrated solar radiation in paraboloidal collectors. *J. Sol. Energy Eng.* 108, 219–225.
- Jeter, S.M., 1986b. Calculation of the concentrated flux density distribution in parabolic trough collectors by a semifinite formulation. *Sol. Energy* 37, 335–345.
- Jiang, S.L., Hu, P., Mo, S.P., Chen, Z.H., 2010. Optical modeling for a two-stage parabolic trough concentrating photovoltaic/thermal system using spectral beam splitting technology. *Sol. Energy Mater. Sol. Cells* 94, 1686–1696.
- Kalogirou, S.A., 2004. Solar thermal collectors and applications. *Prog. Energy Combust. Sci.* 30, 231–295.
- Khanna, S., Kedare, S.B., Singh, S., 2013. Analytical expression for circumferential and axial distribution of absorbed flux on a bent absorber tube of solar parabolic trough concentrator. *Sol. Energy* 94, 26–40.
- Khanna, S., Singh, S., Kedare, S.B., 2015. Explicit expressions for temperature distribution and deflection in absorber tube of solar parabolic trough concentrator. *Sol. Energy* 114, 289–302.
- Khanna, S., Sharma, V., Kedare, S.B., Singh, S., 2016. Experimental investigation of the bending of absorber tube of solar parabolic trough concentrator and comparison with analytical results. *Sol. Energy* 125, 1–11.
- Nicolas, R.O., Duran, J.C., 1980. Generalization of the two-dimensional optical analysis of cylindrical concentrators. *Sol. Energy* 25, 21–31.
- Price, H., Lupfert, E., Kearney, D., Zarza, E., et al., 2002. Advances in parabolic trough solar power technology. *J. Sol. Energy Eng.* 124, 109–125.
- Riveros, H.G., Oliva, A.J., 1986. Graphical analysis of sun concentrating collectors. *Sol. Energy* 36, 313–322.
- Schiel, W., 2012. Collector development for solar parabolic trough power plants. *Bautechnik* 89, 182–191.
- Shuai, Y., Xia, X.L., Tan, H.P., 2008. Radiation performance of dish solar concentrator/cavity receiver systems. *Sol. Energy* 82, 13–21.
- Silverio, G.C., Antonio, B.G., Celestino, O., 2012. Estimating intercept factor of a parabolic solar trough collector with new supporting structure using off-the-shelf photogrammetric equipment. *Appl. Energy* 92, 815–821.
- Tian, Y., Zhao, C.Y., 2013. A review of solar collectors and thermal energy storage in solar thermal applications. *Appl. Energy* 104, 538–553.
- Vijay, D., Mansoor, A., Soma, S.S., et al., 2013. Solar energy: trends and enabling technologies. *Renew. Sustain. Energy Rev.* 19, 55–564.
- Wang, F.Q., Shuai, Y., Yuan, Y., Liu, B., 2012. Effects of material selection on the thermal stresses of tube receiver under concentrated solar irradiation. *Mater. Des.* 33, 284–291.
- Wang, F.Q., Lin, R.Y., Liu, B., Tan, H.P., Shuai, Y., 2013. Optical efficiency analysis of cylindrical cavity receiver with bottom surface convex. *Sol. Energy* 90, 195–204.
- Wu, Z.Y., Li, S.D., Yuan, G.F., Lei, D.Q., et al., 2014. Three-dimensional numerical study of heat transfer characteristics of parabolic trough receiver. *Appl. Energy* 113, 902–911.
- Yang, B., Zhao, J., Xu, T., Zhu, Q., 2010. Calculation of the concentrated flux density distribution in parabolic trough solar concentrators by Monte Carlo Ray-Trace method. In: *IEEE Transactions on Symposium on Photonics and Optoelectronics, SOPO*.
- Zhao, D.M., Xu, E.S., Wang, Z.F., Yu, Q., et al., 2016. Influences of installation and tracking errors on the optical performance of a solar parabolic trough collector. *Renew. Energy* 94, 197–212.